ELSEVIER

International Journal of Mass Spectrometry 181 (1998) 67–87

International Journal of Mass Spectrometry

Properties and performance of a quadrupole mass filter used for resonance ionization mass spectrometry

K. Blaum[a,*], Ch. Geppert[a], P. Müller[a], W. Nörtershäuser[a], E.W. Otten[a], A. Schmitt[a], N. Trautmann[b], K. Wendt[a], B.A. Bushaw[c]

[a]*Institut für Physik and* [b]*Institut für Kernchemie, Johannes Gutenberg-Universität Mainz, D-55099 Mainz, Germany*
[c]*Pacific Northwest National Laboratory, Richland, WA 99352, USA*

Received 25 May 1998; accepted 2 September 1998

Abstract

The performance of commercial quadrupole mass spectrometers (QMS) with a number of imperfections, as compared to the ideal hyperbolic geometry, has been characterized using the computer simulation program SIMION 3D version 6.0. The analysis of simulated QMS geometries focuses primarily on modeling of the internal potential, the study of field deviations, and the influence of finite length on performance of the QMS. The computer simulation of ion trajectories in the QMS field yields predictions for optimum working conditions and provides estimates for the resolving power and the maximum isotopic abundance sensitivity. Experimental measurements that confirm these expectations are presented. Optimization of the geometry and various operational parameters of the QMS is an important step in the development of a system for highly selective ultratrace determination using laser-based resonance ionization mass spectrometry. (Int J Mass Spectrom 181 (1998) 67–87)

Keywords: Computer simulation; Ion trajectories; Isotopic abundance sensitivity; Quadrupole mass spectrometer; Resonance ionization mass spectrometry

1. Introduction

Since Paul and Steinwedel [1] first described the quadrupole mass spectrometer (QMS) in 1953, many theoretical and experimental papers on the basic characteristics of the device [2–14], computer simulations on the field geometry and the ion motion inside the QMS field [15–18], and several reviews as well as text books [19–23] have been published on the subject. Because of its outstanding features concerning performance and applicability, its low cost, and small size, the quadrupole mass filter has rapidly become an extraordinarily useful device, nowadays employed as a standard tool for a multitude of applications in analytical chemistry.

Our particular field of interest is the utilization of a well adapted QMS for resonance ionization mass spectrometry (RIMS) [24–29]. Here a number of advantages is expected when using a QMS in respect to magnetic sector field (MSF) or time of flight (TOF) instruments: (1) The QMS resolution and abundance sensitivity drastically surpasses the value of TOF systems. (2) Background from residual gas collisions

* Corresponding author.

1387-3806/98/$19.00
PII S1387-3806(98)14174-X

is strongly suppressed in comparison to both TOF and MSF spectrometers. (3) The low acceleration voltage at the ionization region of a QMS is well suited to the requirements of narrowband cw laser resonance ionization. (4) Rapid switching between masses without magnetic hysteresis, even allowing transmission of an extended or unlimited mass range, is possible only in the QMS. (5) Finally the small size and price of a QMS favours its use.

Because of these specialized features the successful application of a QMS in a setup dedicated to provide extremely high isobaric and isotopic selectivity is expected by combination with multistep cw resonance ionization on a thermal atomic beam. Presently a bench-scale system is under development in our laboratory for selective ultratrace determination of rare stable and long-lived radioactive isotopes [29,30]. The most demanding application foreseen is ^{41}Ca-determination for radiodating, where isotopic selectivity of greater than 10^{12} and an overall efficiency approaching 10^{-3} are required [31]. Here RIMS with a QMS is expected to become a complementary technique to accelerator mass spectrometry (AMS) [32]. While the characteristics of the laser-based ionization process have been discussed elsewhere [25,33,34], in this article the QMS is analyzed in detail with respect to optimize its basic characteristics of resolution, isotopic abundance sensitivity, and background. In addition to the relevance for the device to RIMS, the investigations are furthermore motivated by the fact that recently serious deficiencies in the performance of commercial QMS systems as compared to ideal expectations were reported [12].

Following a brief outline of the basic theory for the QMS the main part of this work presents the analysis of the characteristics for two different commercially available quadrupole mass filter designs, both are using circular rods of comparable dimensions, and compares them to the ideal hyperbolic QMS geometry. To estimate the performance of the circular rod QMS, the computer simulation package SIMION 3D version 6.0 has been used, which allows full three-dimensional spatial, as well as frequency and phase sensitive, time-dependent simulations of ion motion inside given electric and magnetic fields [35]. The simulation package provides flexible input to address a variety of applications: Potential distributions, ion motion, and transmission efficiency for ions on both stable and unstable trajectories can be estimated. The latter determines the isotopic abundance sensitivity achievable and is evaluated as a function of various operating conditions. In addition, the accepted extraction volume of the ion source, respectively the laser ionization region and the optimum entrance conditions for the ions are derived. The second part of this paper discusses experimental results obtained on a commercial QMS system (ABB Extrel, Pittsburgh, USA, model MEXM 64). Details of the QMS geometry and operating characteristics are given in Table 1. Measurements were performed with a standard crossed-beam electron impact ion source, and isotopic abundance sensitivity as well as resolution have been extracted and are compared to the computer simulations. During these studies, most of the experimental work was carried out in the mass range of calcium (39 and 49 u), as calcium is an ideal test element with six stable isotopes ranging in abundance from 97% for ^{40}Ca down to 32 ppm for ^{46}Ca. Natural abundances of all stable calcium isotopes are given in Table 2 [36]. In addition to the stable isotopes, the long-lived radionuclide ^{41}Ca ($t_{1/2} = 1.03 \times 10^5$ *a* [37]) is included, which is formed in cosmic ray interactions (thermal neutron capture by ^{40}Ca) at the earth's surface with estimated isotopic abundance of 8×10^{-15} [38].

Table 1
Characteristics of the commercial quadrupole mass spectrometer used in the simulations and experiments

QMS characteristics	Dimensions
Circular rods, radius	$r_0 = 8.33$ mm
Free field radius	$R = 1.127\ r_0 = 9.39$ mm
Four grounded stabilizer rods on the 45° axes, radius, location	$r_{stab} = 2.38$ mm at $2.28\ r_0 = 19.05$ mm
Grounded housing, internal radius	$r_{shield} = 4.27\ r_0 = 35.57$ mm
Length of rod system	$L = 210$ mm
Radiofrequency	$\nu = 2.9$ MHz
Upper mass limit	64 u

Table 2
Isotope abundances in naturally occurring calcium (from [36])

A	Abundances (atom %)
40	96.982 (6)
41	8×10^{-13}
42	0.642 14 (4)
43	0.122 40 (2)
44	2.0567 (1)
46	0.003 122 (6)
48	0.182 49 (5)

2. Theory

An ideal quadrupolar geometry is formed by four hyperbolic electrodes of infinite length with two perpendicular zero-potential planes that lie between the electrodes and intersect along the center-line z-axis. As early as 1954, studying the magnetic quadrupole, Dayton et al. [39] discussed the possibility of replacing the hyperbolic electrodes by ones with circular cross section. This approach was adopted by Paul, Reinhard and von Zahn [3] for the electrostatic quadrupole. The detailed theory of this quadrupole mass filter was later developed by Brubaker [6], and an exemplary textbook describing the advantages, as well as shortcomings, of the device has been written by Dawson [22]. The further development from linear to three-dimensional quadrupole traps is reviewed, e.g. by March et al. [23]. The geometry of a QMS with circular cross-section electrodes is shown in Fig. 1, with the two-dimensional inset indicating the polarity of the static (dc) potential used throughout this work: positive dc potential is applied to the two poles in the horizontal x-direction, while negative dc potential (of equal magnitude) is applied to the two poles in the vertical y-direction.

For mass analysis both a static electric (dc) potential and an alternating (ac) potential in the rf range are applied to the electrodes of the QMS. The relative amplitudes of the dc and ac potentials control the ability of the system to mass filter a low energy beam of ions travelling along the z-axis. Assuming idealized field conditions within the structure, with vanishing component in the z direction, the potential distribution $\Phi(r, t)$ is given by

$$\Phi(r, t) = \Phi_0(t) \frac{(x^2 - y^2)}{r_0^2} \tag{1}$$

and

$$\Phi_0(t) = U + V \cos(\omega t) \tag{2}$$

where U is the amplitude of the static dc potential and V is the amplitude of the rf potential, which oscillates

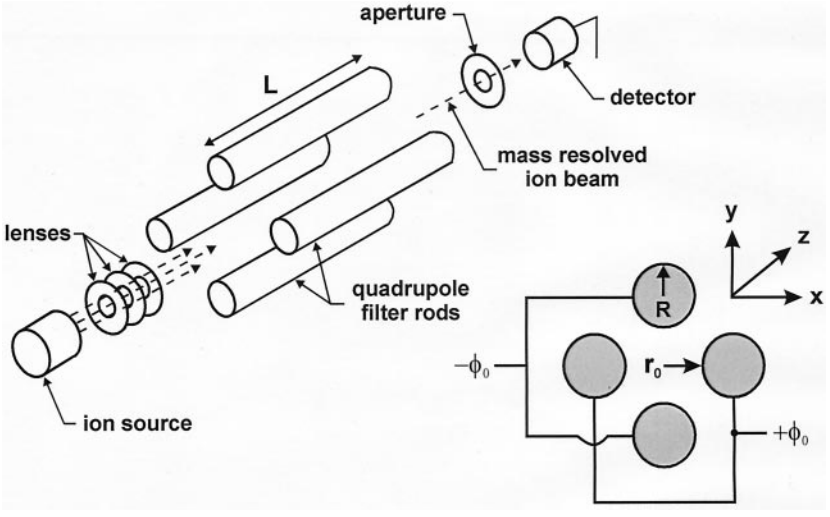

Fig. 1. Schematic diagram of the typical QMS consisting of ion source, rod system, and detector. The inlay denotes the polarity of the dc potential Φ_0 with respect to the cartesian coordinates x and y, the free field radius r_0, and the rod radius R.

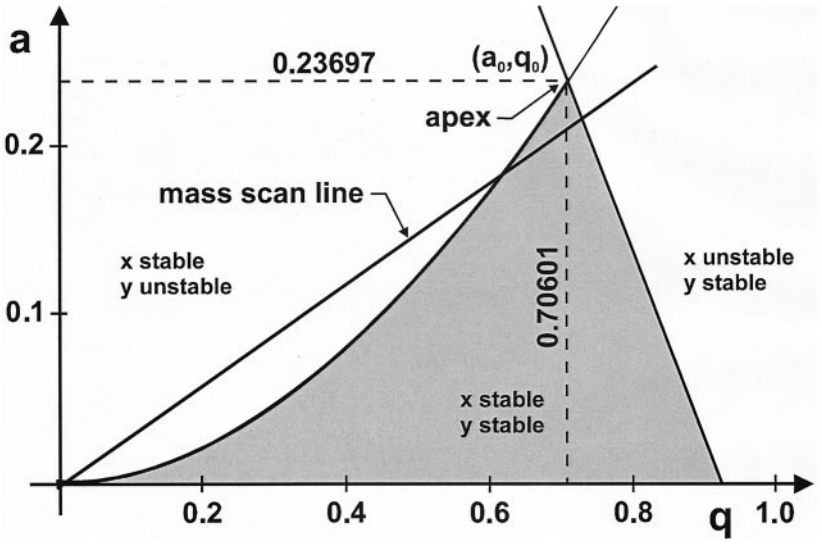

Fig. 2. First Mathieu stability region in the (a, q)-plane. Regions of stability and instability are labelled, the position of the apex and a typical mass scan line are given.

with angular frequency $\omega = 2\pi\nu$. In case of a perfectly hyperbolic QMS geometry the radius r_0 is defined by the circle tangential to the four hyperbolic electrodes, and is known as the free field radius. The first two Cartesian coordinates, x and y, are as shown in Fig. 1. The potential (1) satisfies the Laplace equation $\nabla^2\Phi = 0$ and is invariant in the z direction. A single ion passing through the device undergoes a motion that is a solution of Mathieu's equations [40]

$$\frac{d^2u}{d\xi^2} + [a_u - 2q_u \cos(2\xi)]u = 0 \tag{3}$$

where $\xi = \omega t/2$ and u represents the x or y displacement of the ion in two distinct equations; one for each dimension. The parameters a_u and q_u are related to the potentials U and V by:

$$a_u = a_x = -a_y = \frac{8eU}{mr_0^2\omega^2}$$

$$q_u = q_x = -q_y = \frac{4eV}{mr_0^2\omega^2} \tag{4}$$

where m is the ion mass and e the elementary charge. In this work only singly charged ions are considered. The solutions of Mathieu's equations for motion in the x–y plane contain either a strictly growing exponential factor or an oscillatory term of finite radial extent, depending on the ion mass m. Mathieu's stability diagram for the (a, q)-plane, as shown in Fig. 2, illustrates the manner in which the filter is operated. The Mathieu equation solutions are characterized as being stable or unstable. For the sake of clarity only the first region of stability is considered in this work; discussion of other regions of stability can be found in [13,14,22]. With proper choice of a and q, or U and V, respectively, somewhere in the shaded stable region, ions of a corresponding m have stable trajectories, i.e. they oscillate around the z axis with finite amplitude and ultimately emerge from the end of the mass filter. For (a, q)-values outside this stable region, i.e. ions with lower or higher masses, the ion motion is unstable, either in the x direction, in the y direction, or in both; hence, the ions steadily move away from the z axis during oscillation and ultimately strike the electrodes being removed. Fig. 3 presents typical stable ion trajectories in the x- and y-coordinate calculated for (a, q)-parameters of (0.23, 0.706) near the apex of the stability region. The entrance parameters were $x = y = 0.5$ mm off-axis, starting angle 0°, and phase angle (relative to the rf-field) of

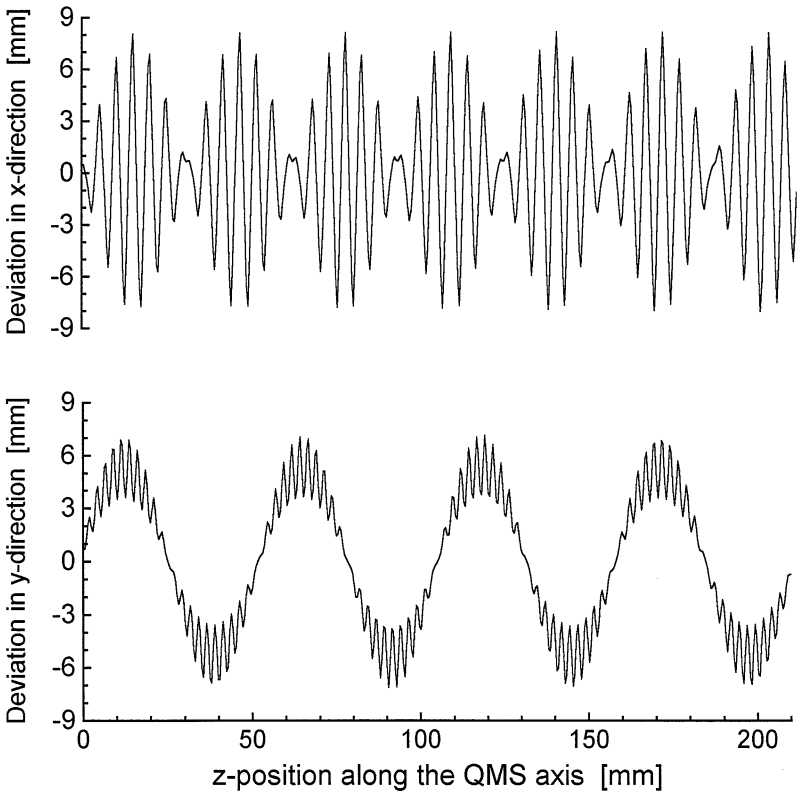

Fig. 3. Projection of a 3D trajectory simulation of a stable ion onto the *x*- and *y*-coordinate. The macro- and the micro-oscillations in the ion motion are clearly visible.

0°. It should be noted that even though the ion enters the QMS field very close to the axis, the maximum oscillation amplitude is ~8 mm, more than 15 times the starting parameter and reaches the full free field radius, i.e. the distance to the electrodes. Operating under conditions of near critical stability, such as those considered here, only ions with a very small entrance deviation have oscillation amplitudes sufficiently small to be transmitted through the QMS. Simultaneously scanning the amplitudes of U and V along a "mass scan line" of fixed ratio of $U/V = a/2q$, as indicated in Fig. 2, gives the mass spectrum. Alternatively, the mass spectrum could also be obtained by variation of the radiofrequency ν with fixed amplitudes of U and V, however, this is very uncommon in practice because of instrumental complications.

The construction of QMS filters using electrode rods with circular cross section, rather than the ideal hyperbolic cross section, dramatically simplifies fabrication and mounting of the system and is standard for commercial designs. Field errors caused by this substitution are generally reduced by optimizing the rod radius with respect to the free field radius. Paul and other authors have presented elaborate analytical, semi-analytical and numerical calculations that yielded approximations for optimizing operating parameters and performance of a QMS with circular cross-section electrodes [3,9,10,12,22]. More recently, computer simulations and theoretical studies have been used to obtain precise information about the behavior of the QMS [13–18].

The potential distribution in the *x*-*y* plane of the quadrupole with circular rods can be expressed as an infinite multipole expansion, written in cylindrical coordinates [9] as:

$$\Phi(r, t) = [U + V\cos(\omega t)] \sum_{m=0}^{\infty} C_m \left(\frac{r}{r_0}\right)^m \cos(m\theta) \tag{5}$$

where $\theta = \arctan(y/x)$. Terms containing r^{-m} do not appear, because $\Phi(r) = 0$ must be satisfied on the axis. Eq. (5) is also a solution of Laplace's equation. In case of perfect fourfold symmetry where all four rods have identical radius R and are located precisely at distance r_0 from the z axis, the potential changes sign when θ changes by $\pm\pi/2$. Thus, the condition

$$\cos\left(m\,\frac{\pi}{2}\right) = -1 \tag{6}$$

must be fulfilled, which implies that the expression for the potential contains only terms with $m = 2, 6, 10, 14, \ldots$, or written in generalized form

$$\Phi(r, t) = [U + V\cos(\omega t)] \sum_{n=0}^{\infty} C_n \left(\frac{r}{r_0}\right)^{2(2n+1)} \times \cos[2(2n + 1)\theta] \tag{7}$$

The first term in this multipole expansion is the quadrupole term, the second is a 12-pole term, the third is a 20-pole term, etc. To derive the equations of motion, relation (7) must be differentiated. In rectangular coordinates the solutions are:

$$\frac{d^2x}{d\xi^2} = -[a + 2q\cos(2\xi)] \sum_{n=0}^{\infty} C_n(2n + 1) \times \left(\frac{x^2 + y^2}{r_0^2}\right)^{2n} \times \{x\cos[2(2n + 1)\theta] + y\sin[2(2n + 1)\theta]\} \tag{8}$$

$$\frac{d^2y}{d\xi^2} = -[a + 2q \times \cos(2\xi)] \sum_{n=0}^{\infty} C_n(2n + 1) \times \left(\frac{x^2 + y^2}{r_0^2}\right)^{2n} \times \{y\cos[2(2n + 1)\theta] - x\sin[2(2n + 1)\theta]\} \tag{9}$$

where ξ, a and q are as given above for Eq. (3) and (4). It is of value to note that the quadrupole term ($n = 0$) for each equation depends only on a single coordinate rather than on both x and y. In contrast, higher multipole terms of Eqs. (8) and (9) are related to both coordinates x and y. Thus, in a quadrupole structure with circular electrodes, the components of the ion motion in the x and y direction are no longer independent but coupled by higher order field components. The best approximation to a pure quadrupolar potential is the choice of electrode radius R such that $C_1 = 0$ to remove the 12-pole contributions. The technique of determining the values of the coefficients C_n, as a function of electrode radius is given in [9]. Dayton et al. [39] were first to empirically determine the optimum radius of the circular electrodes to be $R_{opt} = 1.148\ r_0$. Unfortunately, the paper by Paul et al. [3] misquoted Dayton by giving $R_{opt} = 1.16\ r_0$ and many authors have subsequently used this slightly wrong value in referring to [3]. In practice, the quadrupole rods are mounted within a grounded housing, which is only slightly larger than the electrode structure itself, and thus contributes to the potential distribution. Being radially symmetric, this contribution has only little influence on the optimum rod size but strongly increases the electric field gradient close to the two 45° planes between the rods [9]. In 1971 Lee-Whiting et al. [10] published a refined value of $R_{opt} = 1.145\ 11\ r_0$, obtained by semianalytical calculations. With this value, the first nonvanishing perturbing term in Eq. (7) is that with $n = 2$, the 20-pole term. This contribution (and that of higher order terms) is negligible near the z-axis of the quadrupole, but becomes significant in close vicinity to the rods. A consequence of these higher multipole orders is the appearance of nonlinear resonances, or so-called stop-bands. These effects are well known in quadrupole ion traps [23,41], where they have been subject of detailed investigations recently [41–43]. In linear QMS they may lead to reduction of transmission for certain values of (a, q) and impose structure on the peak shapes observed in mass spectra [5,22]. However, only minor effects are expected in the QMS designs considered here which will be discussed in a forthcoming paper.

A dominant limitation of a laboratory QMS, as compared to an idealized geometry, is the finite length of the rods. To obtain a high level of mass selection, virtually all ions with incorrect value of m must experience a sufficiently strong transversal acceleration and must remain in the field long enough to be rejected. Paul et al. [3] postulated a simple relationship between the maximum achievable resolving power $\mathcal{R}_{\max}$ and the number of rf-cycles N experienced by the ions while traversing the device:

$$\mathcal{R}_{\max} = m/\Delta m \approx N^2/12.25 \tag{10}$$

where Δm is the full width at half maximum (FWHM). This guess is supposed to be valid for reasonable transmission and has been confirmed by a number of other works (see e.g. [22] and references therein). It is based on the fact that in a high-resolution mode the mass scan line lies very close to the apex of the stability diagram and the micro-oscillation of the ion in the y direction is almost synchronous to the rf field frequency ν. The number of rf cycles can be increased by decreasing the axial velocity of the ions, increasing ν, and/or increasing the rod length. Thus:

$$N = \nu t \approx \nu L \sqrt{m/2E} \tag{11}$$

For a QMS of a given length L this sets an upper limit on the maximum axial ion energy $E_{\max}$ for a given resolution $\mathcal{R}_{\max}$:

$$\mathcal{R}_{\max} \approx 0.0426 L_{\mathrm{cm}}^2 \nu_{\mathrm{MHz}}^2 m_u / E_{\max,\mathrm{eV}} \tag{12}$$

Thus, maximizing $\mathcal{R}$ for a given QMS length implies the choice of a high radiofrequency and an ion entrance energy as low as possible. For example, to achieve $\mathcal{R}_{\max} > 1000$ at mass number 40 using the operating parameters given in Table 1 requires $E_{\max} < 6$ eV.

Well below the limiting condition of (12), the mass resolution is determined from the experimental settings using the relations of an ideal, infinitely long QMS, derived from the two points where the mass scan line intersects the stability curve. This value is given by the simple analytical expression [3]

$$\mathcal{R} \approx \frac{0.126}{0.16784 - U/V} = \frac{0.126}{(0.16784 - \gamma) + \delta/V} \tag{13}$$

The resolution can be varied via the ratio U/V, i.e. the slope of the mass scan line, measured in fractions of the factor $0.167\ 84 = a_0/2q_o$. Experimentally, this is usually accomplished by adjustment of the relation $U = \gamma\ V - \delta$, where the operating parameter γ controls the resolution and the parameter δ is an added dc offset. For $\delta = 0$, constant $m/\Delta m$ resolution mode is obtained. Approaching the value of $U/V = 0.16\ 784$, corresponding to a mass scan line slope of 1, would yield highest mass resolution, limited by Eq. (12) for real systems. With the choice of $\gamma = 0.167\ 84$ and $\delta \neq 0$, the resolution $m/\Delta m$ becomes proportional to V and hence also proportional to m. This is the condition for a constant Δm mode, where the width of the transmitted mass peak is constant and independent of the mass m. In practice, a QMS is normally operated somewhere between these two modes and often even a variation in the ratio U/V is performed during a mass scan to correct for mass discrimination effects [22].

3. Simulations

3.1. Program description and procedure

To predict the performance of different QMS-designs in this work, the software package SIMION 3D version 6.0 [35] was used. SIMION 3D is a PC-based ion trajectory tracing tool designed to model ion optics problems within three-dimensional (3D) electrostatic and/or magnetic potential arrays. The specific method used by the SIMION routines to solve the Laplace equation is a finite difference technique called over relaxation. To simulate time-dependent devices, such as a radiofrequency driven quadrupole electrode structure, SIMION 3D allows the incorporation of real-time user programs. Corresponding subroutines were written by us providing flexible variation and control of the major input parameters: dc voltage, rf voltage, radiofrequency and rf phase, ion mass and initial energy, starting point, velocity, and initial angle. We

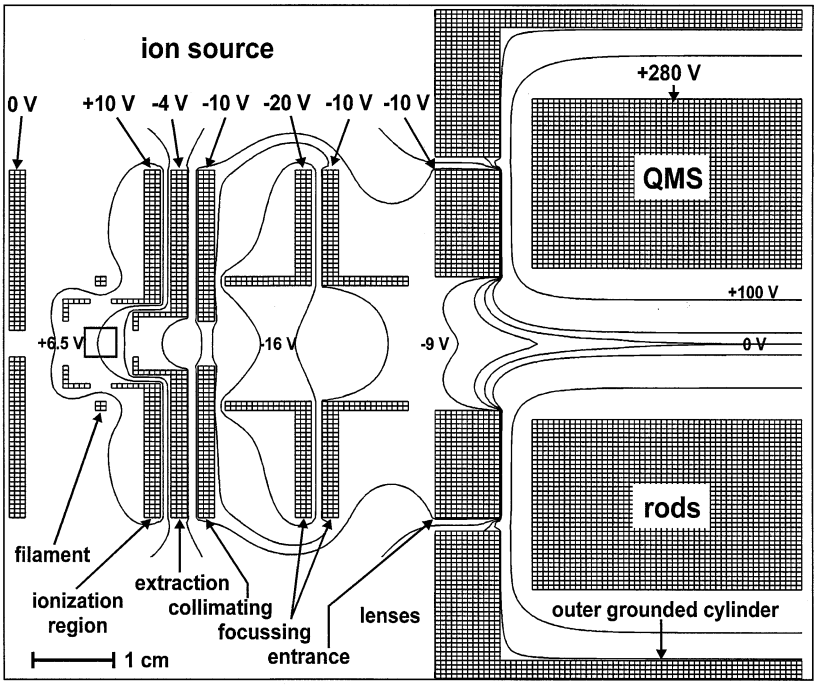

Fig. 4. Schematic diagram of the electron impact ion source with equipotential contour lines for typical working conditions.

have treated the three major parts of the quadrupole mass filter system individually, each in a fully three-dimensional representation and calculation: (1) the ionization region and entrance ion optics, (2) the quadrupole region itself and (3) the detector region. In this way, maximum resolution in the potential arrays and the resulting ion trajectories was achieved. Choosing large overlaps of up to 25% between the different 3D potential arrays ensured that the interactions of the different potentials and influences from fringing fields on ion trajectories were properly taken into account.

3.2. Ion source

The acceptance of the QMS was determined by a dynamical 3D simulation of the ion source and entrance optics, including the first part of the QMS rods. This calculation yielded the size and location of the ion source volume from which ions are extracted and successfully transmitted into the QMS, giving predictions for the optimum entrance conditions. Fig. 4 shows the geometry of the standard crossed-beam electron impact ion source that was modelled, including (1) the filament and the resulting electron beam passing through the ionization region, (2) the extraction electrode for the positive ions, (3) three lenses for collimating and focussing, and (4) an entrance lens for fringing field compensation. The electron beam of about 1 mA current is directed vertically, perpendicular to the trajectories of the ions. Space charge effects have been considered, but give only minor contributions. Fig. 4 also shows potential contour lines for typical optimized working conditions of the ion source and ion optics settings. Using the potentials shown as labels in Fig. 4, the ionization volume, from which ions are extracted by the ion optics and subsequently accepted by the QMS without significant transmission losses, was determined. This volume is well approximated by a cylinder of 2.9 mm diameter and 4.8 mm length in the middle of the ionization region. Because the low initial (thermal) velocities of the entering atoms compared to the acceleration of 5–15 eV, the ions form a nearly

parallel beam at the QMS entrance plane. Figs. 5(a) and (b) show the corresponding ion source emittance in phase space, which is indicated by the shaded ellipse connecting maximum radial parameters and angles in the entrance plane. Because of the fringing fields experienced by the ions as they enter the QMS, the accepted entrance angle and beam diameter strongly depend on the phase of the rf field. This fact results in phase dependent acceptance ellipses, which have been calculated for seven different phase angles over the range from 0°–180° for both x and y directions and are included in the figures. The overlapping region of the different acceptance ellipses of this particular QMS is well matched to the emittance phase space of the ion source reaching maximum values of 5° and 0.6 mm, respectively. The simulation also shows that the ions experience about two rf oscillations within the destabilizing fringing field before passing the QMS entrance plane. This value gives optimum transmission through the QMS, without significant disturbance on the acceptance, as predicted by Dawson [22]. Our result also confirms earlier computer studies by Brubaker [8], who discussed that influences from fringing fields at the QMS entrance can be minimized by proper choice of the ionization volume and strong focussing in the ion lenses, if sufficiently rapid passage through the fringe field region is provided.

3.3. Potential distribution inside the QMS

As pointed out in Sec. 2, a QMS with circular rods but perfect four-fold symmetry will exhibit field distortions of sixth, tenth, . . . , 2 $(2n + 1)$-order according to Eq. (7). To determine the size of these contributions in comparison to the ideal hyperbolic field, SIMION 3D was used to calculate the radial potential distribution on a 2D grid of 1528×1528 points equally spaced by 50 μm over the QMS electrode structure. The relative difference between the simulated and theoretical values calculated for the ideal hyperbolic potential was less than 10^{-6}, which can be attributed to arithmetic convergence and interpolation error, and is negligible compared to the field distortions observed with circular rod geometries. Figs. 6(a) and 7(a) show a set of equipotential lines resulting for the electrode structure of two commercially available QMS types, both with circular rods. The quadrupole designs differ in the choice of the ratio of rod radius R to free field radius r_0. With $r_0 =$ 8.33 mm in both cases, the design of Fig. 6(a) has $R = 1.16\ r_0$, while the geometry in Fig. 7(a) has $R = 1.127\ r_0$ and includes four additional grounded stabilizer rods of $r_{\mathrm{stab}} = 4.76$ mm diameter located on the 45° planes at a radius of 19.05 mm. This geometry is identical to that described by the parameters given in Table 1. In both cases an outer grounded shielding cylinder is located on $r_{\mathrm{shield}} = 4.27\ r_0 = 35.57$ mm. The contour plots of Figs. 6(b) and 7(b) show the logarithm of the relative potential difference between the two circular and an ideal hyperbolic quadrupole geometry for an expanded region of one quadrant, as indicated by the squares in Figs. 6(a) and 7(a). In the central region, near the quadrupole axis, the relative potential deviations in both cases are on the order of 10^{-3}. Following increasing r in the vicinity of the 45° symmetry line, the potential differences pass over a narrow saddle-shaped region of nearly perfect approximation of better than 10^{-4}, which extends from $\sim 0.7\ r_0$ at 45° over an angle of $\pm 20°$ down to the rods. Further out, the potential discrepancy grows rapidly and reaches more than 10% between the rods. In the central region of $r < 0.7\ r_0$, deviations are introduced predominantly by the sixth order distortion. Here, the averaged deviation for the standard design of Fig. 6(a) is about 3×10^{-3}. Slightly changing the ratio of R/r_0 and adding the stabilizer rods reduces this quantity by more than a factor of 6, down to less than 5×10^{-4}. Even over the complete region out to radius r_0 the desired quadrupole potential distribution in Fig. 7(b) with the stabilizer rod design is still better by about a factor of 3. In the contour plots for both designs, lighter shaded areas of worse approximation are observed near the rods at angles of 18° and 72° with respect to the x-axis. These are caused by the potential distortion of tenth order with comparable magnitude of about 10^{-2} deviation for both designs, but with a considerably smaller spatial extent in the stabilizer rod design. It is worthwhile to note that the high resolution in the electrode definition grid of more

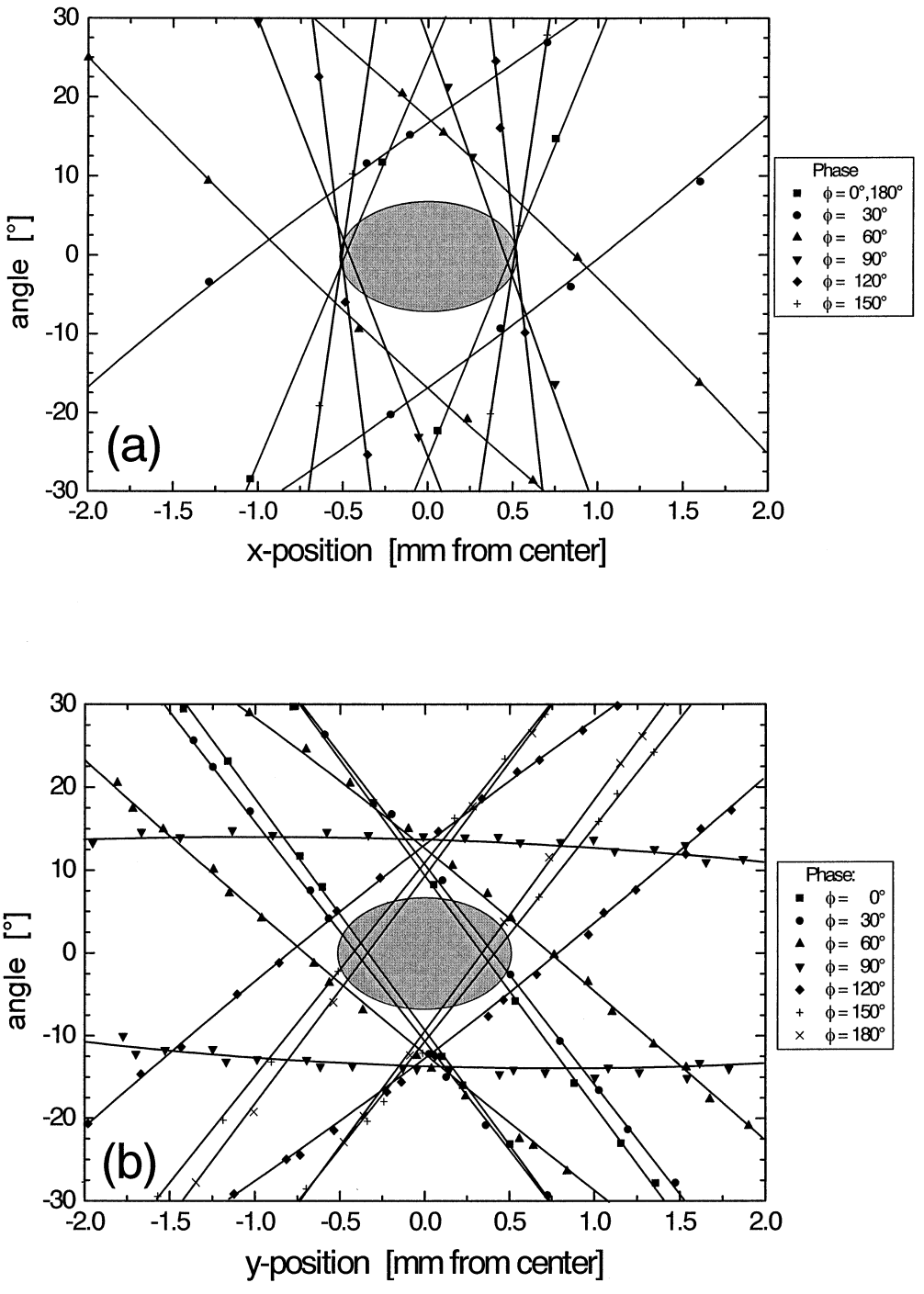

Fig. 5. Emittance ellipses of the ion source (shaded areas), as compared to the overlap of the phase dependent acceptance ellipses of the QMS, calculated for 7 rf phases from 0°–180°. (a) *x*-direction, (b) *y*-direction.

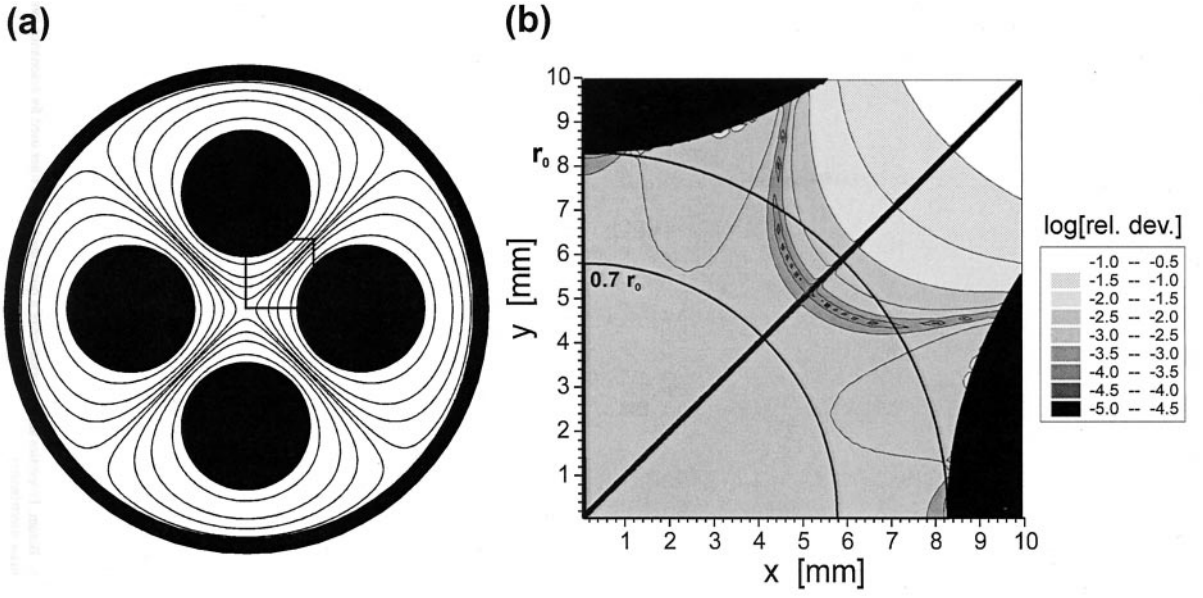

Fig. 6. (a) The potential distribution in a circular cross-section electrode quadrupole with rod radii of $R = 1.16\ r_0$ within a cylinder at zero potential. (b) Logarithmic contour plot of the relative potential difference between the simulated real and the ideal quadrupole potential for the marked quadrant indicated in (a).

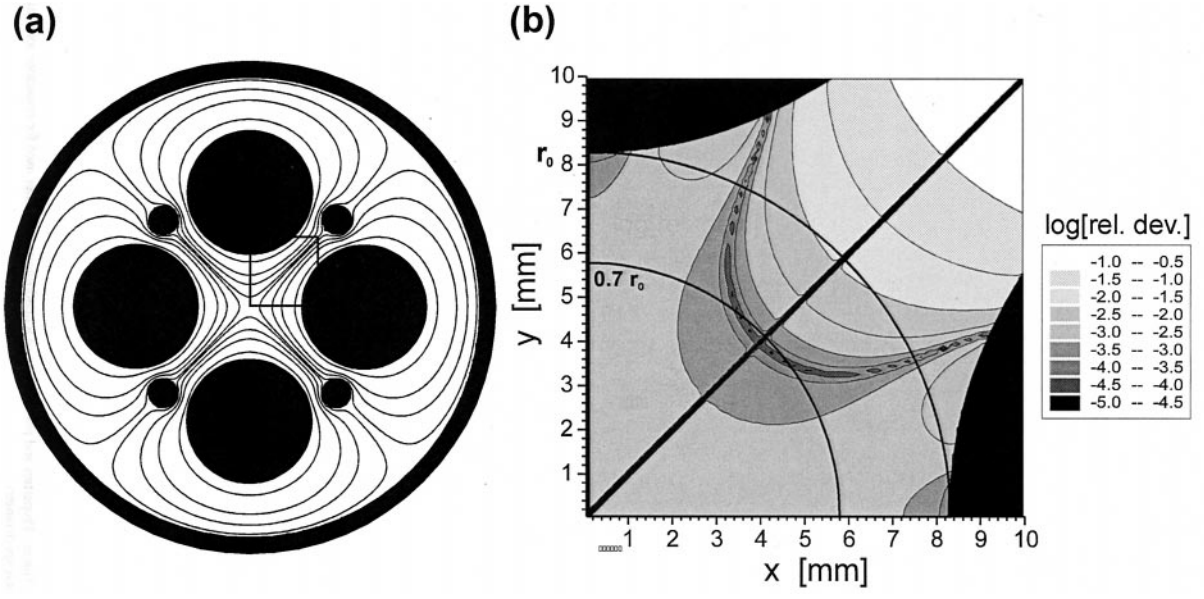

Fig. 7. Diagrams similar to those described in Fig. 6(a) and (b), but for a circular cross-section electrode quadrupole with rod radii of $R = 1.127\ r_0$ and grounded stabilizer rods.

Table 3
(a_0, q_0)-values of the apexes of the stability diagrams for a theoretical quadrupole field compared with the results from the SIMION 3D simulations for three different quadrupole designs

		Simulations		
Parameter	Theory [22]	Hyperbolic	Circular, $R = 1.16\ r_0$	Circular, $R = 1.127\ r_0$ + stabilizer rods
a_0	0.236 97	0.2370	0.2384	0.2374
q_0	0.706 01	0.7060	0.7104	0.7074

than 10^6 points is required for these calculations to avoid artifacts caused by inaccurate approximation of the potential boundaries, i.e. the QMS rods.

3.3.1. Stability diagram

The Eqs. of motion for the QMS (8) and (9) result in stable ion trajectories only for certain values of a and q, which differ only slightly from those of the ideal QMS. To investigate these changes, we determined the limits of ion trajectory stability by SIMION 3D simulations for a number of different slopes of the mass scan line close to maximum resolution such that the uppermost apex of the stability diagram was utilized. This analysis was performed applying the simulation of 3D ion motion inside the QMS for both circular geometries as well as the ideal hyperbolic electrodes. Remarkably, the stability diagrams for the three different designs appear to be geometrically indistinguishable, with only very slight shifts of a and q to higher values, i.e. towards smaller masses, for both circular rod QMS designs. The (a_0, q_0)-values of the apexes of the stability diagrams, as extracted from the simulations, are listed in Table 3 for the three quadrupole designs together with the direct calculation for the hyperbolic field. The excellent agreement of the (a_0, q_0)-value between simulation and theory for the hyperbolic quadrupole demonstrates the high accuracy of the simulation and gives confidence to the results for the other geometries. The deviation of the apex values from the theoretical hyperbolic value for the two commercial designs is very small; about 0.7% for the simple circular rod design and less than 0.2% using the smaller R/r_0-ratio and stabilizer rods. While these shifts in apex values are of little consequence for practical operation, nonlinearities in the stabilizing force of a QMS do have an additional influence on the ion motion. This is demonstrated in Fig. 8, which compares the y-component of a typical ion trajectory for the ideal and the circular rod QMS. In the circular geometry, there is a clear reduction in the frequency of the ion macromotion, arising from a lowered refocusing force in the vicinity of the rods. This effect leads to a higher probability of finding the ion far off axis and thus may lead to reduced transmission.

3.3.2. Resolution

For sufficiently high slope of the mass scan line, the finite length of the QMS poses the major limitation on the achievable resolution. Fig. 9 shows the number of rf cycles N experienced by a singly charged ion traversing a QMS of finite length, given as a function of ion entrance energy E. The results are calculated in two distinct ways: The line results from Eq. (12) together with the experimental parameters of $L = 21$ cm, $\nu = 2.9$ MHz and $m = 40$ u, while the symbols are extracted from the y-direction oscillation of the simulated ion trajectory, which is expected to be governed by the radiofrequency. The excellent agreement confirms the simple relationships given in Eqs. (10)–(12) as well as lending further confidence to the simulations. These calculations have been performed for all three QMS designs, discussed above, and yield results that are equal within the size of the symbols. Even though the macromotion of the ion depends strongly on the field geometry, with significant differences for the individual QMS designs, as demonstrated in Fig. 8, the micromotion accurately tracks the radiofrequency. The curve also illustrates graphically the importance of low ion entrance energy for good filter performance. As indicated by the

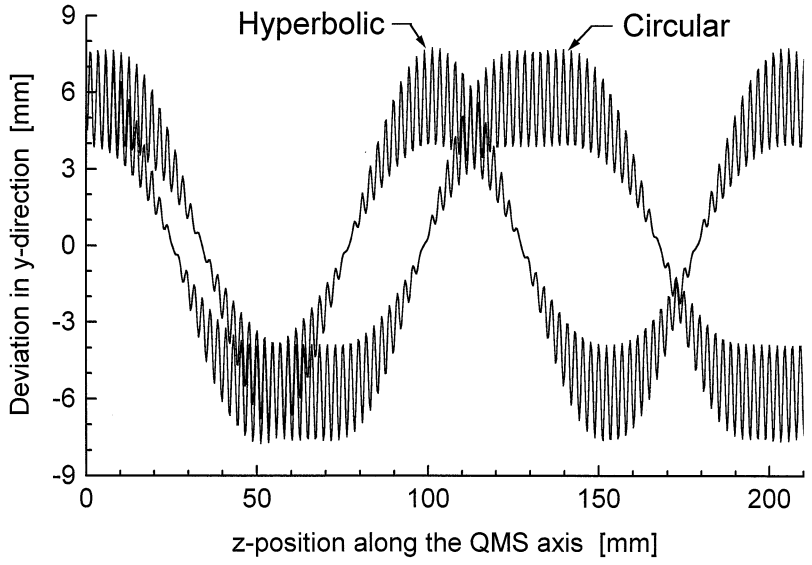

Fig. 8. Motion in the *y*-coordinate for ions travelling through a circular rod QMS compared to an ideal hyperbolic field, showing the reduction in macromotion frequency and increased residence time in the vicinity of the rods.

shaded area, to attain more than 70 rf oscillations, which corresponds to a resolution of $\mathcal{R} \geq 400$, requires ion entrance energies below 15 eV. A somewhat arbitrary lower limit to the range of useful ion entrance energies is set at about 5 eV, below which unacceptably high transmission losses in the ionization and entrance region occur. A completely independent theoretical prediction of the resolution would require an extensive choice of starting conditions with full variation of possible spatial, energetic and angular distribution. This is an extremely time and labor consuming procedure and has not yet been performed.

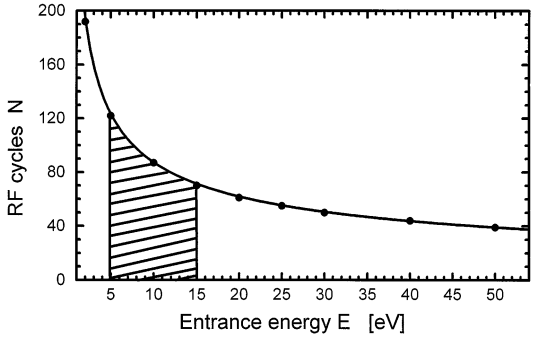

Fig. 9. Calculated (line) and simulated (symbols) relation of rf cycles experienced by the ions as a function of entrance energy. The shaded area marks the region of optimized performance.

3.3.3. Abundance sensitivity

The isotopic abundance sensitivity is one of the most important figures of merit for a mass spectrometer system, particularly if it is to be used for selective ultratrace measurements such as the envisaged RIMS applications. It describes the ability of the system to observe a weak peak directly adjacent to a strong neighboring peak, using the following conceptual definition: It is the minimum detectable mass peak height at the desired mass A divided by the peak height of the dominant neighboring mass at $A + 1$ or $A - 1$; this is also the reciprocal of the neighboring mass suppression S. A more conservative estimate may be obtained from the relative contribution of an interfering mass A at the intermediate position of $A + 1/2$ or $A - 1/2$, respectively. This latter definition has the practical advantage that a value for S can be measured even when isobaric interferences are present at all masses. Furthermore, the neighboring mass suppression S can be treated as a selectivity S, such as is used in optical spectroscopy [44] and other

fields, both written with a positive exponent. The determination at the positions $A \pm 1/2$, half way between the actual mass peaks, will always strongly underestimate the actual unit mass separation selectivity S. However, we shall use this definition in the following discussion to facilitate the comparison of simulation with experiment.

Isotopic abundance sensitivity is obviously dependent on resolution but is even more strongly influenced by the overall shape of the mass peak, especially in the far reaching wings. Thus it cannot easily be calculated from the QMS operating parameters. To our knowledge, no theoretical calculations of isotopic abundance sensitivity for different QMS designs have been performed previously. Our approach to estimating abundance sensitivity is conceptually simple and uses the ion trajectory routine of SIMION 3D: The QMS, set to a given mass number A, has a known acceptance in the x- and y-coordinate for stable transmission, which can be used to define a (usually) ellipsoidal acceptance area denoted M_{stable}. We then select a slope of the mass scan line of sufficiently high value such that tuning the QMS to mass $A + 1/2$ or $A - 1/2$ already produces an unstable trajectory for mass A. For the QMS of finite length, we shall nevertheless find small but finite areas $M_{A+1/2}$ and $M_{A-1/2}$ in close vicinity to the QMS axis where defocussing forces are too small to cause rejection of ions of "unstable" mass A before they reach the detector. The ratio of these "unstable" acceptance areas to M_{stable} is then a direct measure of the mass peak suppression at the position $A + 1/2$ or $A - 1/2$ and hence a good estimate for the isotopic abundance sensitivity. These unstable areas can be extracted from the SIMION 3D simulations by calculating ion trajectories of mass A for the QMS tuned to mass A, $A + 1/2$ and $A - 1/2$ as a function of the entrance position in x and y. For all but vanishingly small x and y starting positions, the unstable trajectories terminate in collisions with the electrodes. However, the relationship between the starting position and the length of the QMS that is traversed before rejection occurs can be extrapolated to the full length of the QMS, and thus determine the limiting maximum x or y values that can (just) traverse the complete length without being rejected. These are then used as the major and minor axes of ellipses used to estimate the areas of $M_{A+1/2}$ and $M_{A-1/2}$. As a further simplification, it is worthwhile to recall that tuning to heavier or lighter neighboring masses produce instability only in one coordinate, thus the "unstable" transmitted areas are very narrow only in this coordinate, but are essentially identical to the stable mass area in the other coordinate. Thus we need only consider the unstable coordinate to obtain the ratio of "stable" to "unstable" area.

Before applying the idea of using acceptance areas to determine selectivity, we must consider the influence of the phase of the rf field on the path length of the rejected ion. Results are shown in Fig. 10 for the three QMS designs: hyperbolic field (A), with circular rods (B) and with additional stabilizer rods (C), all with standard operating parameters of $L = 21$ cm, $r_0 = 8.33$ mm, $\nu = 2.9$ MHz, and resolution adjusted to $\mathcal{R} = 100$. The rf phase variation covers the full range from 0°–360°, while the initial ion entrance conditions were chosen to be $x_0 = y_0 = 0.01$ mm, $E_{\text{axial}} = 5$ eV, and entrance angle of 0°. The quadrupole was tuned to stability for mass $A = 39.5$ u in Fig. 10(a) and for mass $A = 40.5$ u in Fig. 10(b), and then simulations were performed for $A = 40$ u. It is apparent that the distance needed for rejection of a heavier mass $A + 1/2$, which is unstable in y [Fig. 10(a)], is generally about twice as long as that for one of lighter mass $A - 1/2$, which is unstable in x [Fig. 10(b)]. This behavior clearly illustrates the generally observed fact that a QMS provides better suppression of lighter neighboring masses than of heavier ones. Furthermore, the rf phase behavior is distinctly different: For the x direction (lighter mass), the path length before rejection has only one maximum at phase angle 90°, while the y direction (heavier mass) exhibits a second maximum at 270°. This fact is related to the difference in the micromotion which occurs around ν for y and around $\nu/2$ for x (compare Fig. 3) and is also conducive to better rejection of the lighter masses. Because of lower rejecting field experienced in the circular rod QMS, particularly in the vicinity of the rods, the distance travelled before rejection is generally about 1.4 times greater than in the ideal QMS.

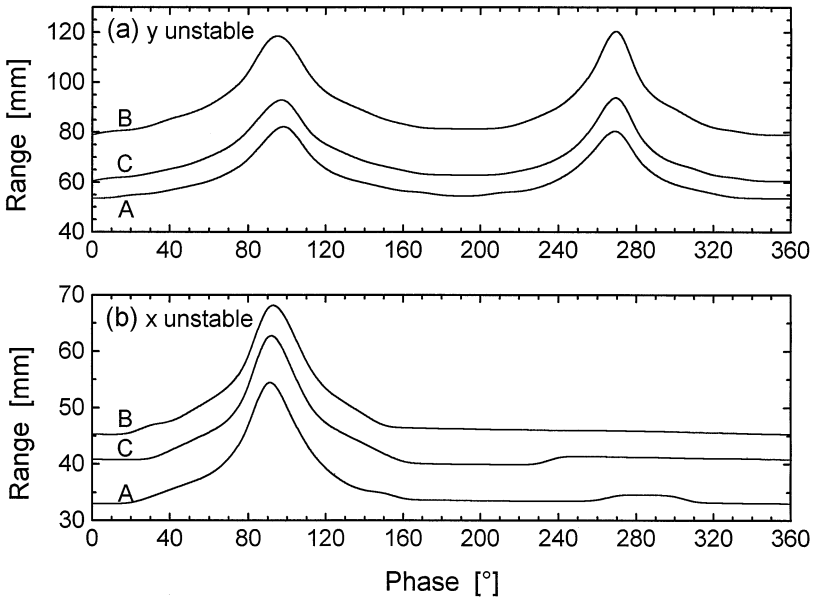

Fig. 10. Simulated path length before rejection for ions of mass $A = 40$ u on unstable trajectories in the three different QMS designs with hyperbolic rods (A), circular rods $R = 1.16\ r_0$ (B), and circular rods $R = 1.127\ r_0$ with stabilizer rods (C), as the rf phase varies from 0°–360°. In (a) the quadrupole was tuned to mass 39.5 u (ions are *x*-stable and *y*-unstable) and in (b) to mass 40.5 u (ions are *x*-unstable and *y*-stable). $x_0 = y_0 = 0.01$ mm; $E = 5$ eV.

The behavior with the stabilizer rods is improved, but is still not as good as the ideal hyperbolic geometry.

Continuing with the concept outlined above for estimating the isotopic abundance sensitivity, we then compute the phase-averaged maximum flight lengths for mass A with the quadrupole tuned to stability at mass $A + 1/2$ and $A - 1/2$, respectively. Simulations were carried out as a function of entrance parameter in the direction of instability, x or y, respectively, for the different QMS designs. Fig. 11 shows the results for ions of mass 40 u with the QMS tuned to stability for either mass 39.5 u [Fig. 11(a)] or 40.5 u [Fig. 11(b)]. All other conditions were chosen similar to those given above: Entrance angle of 0°, ion entrance energy 5 eV, mass resolution 100, and radiofrequency 2.9 MHz. The simulation covers the range of entrance parameter from 0.3 mm down to 10^{-3} mm, which is limited by the SIMION grid size and where a maximum flight length of about 100 mm is reached. As expected from the exponential growth of unstable trajectories, a linear relationship is observed in a semilogarithmic representation, which can easily be fit and extrapolated to the full QMS rod length of 210 mm. Small deviations from linearity are attributed to micromotion of the ions and lead to errors of about 5% in the determined slopes. The extrapolation was performed for all three QMS designs and ratios of the maximum accepted "unstable" entrance value to the known stable entrance area from Sec. 3.2 were obtained for both the lower and heavier mass side. These give the neighboring mass suppression S, i.e. the reciprocal abundance sensitivities at half-mass unit separation, as listed in Table 4. The results computed for suppression of the heavier side of a given mass peak are generally about three orders of magnitude better than on the lower mass side. Here calculations for the ideal hyperbolic geometry predict values up to $S \approx 1 \times 10^{12}$, while the selectivity to the lower side reaches values of $S \approx 9 \times 10^{7}$. This again is the well known characteristic of the QMS with pronounced tailing on the lower side of a mass peak. Values for the different commercial designs are significantly lower in both cases.

To evaluate the influence of the experimental

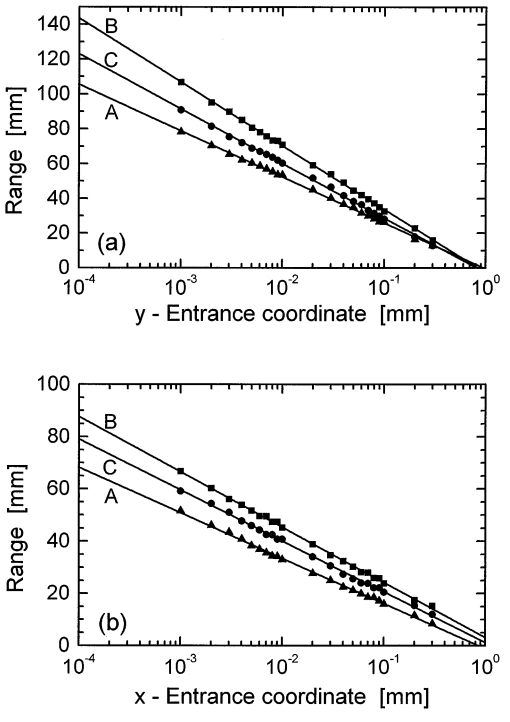

Fig. 11. Phase-averaged trajectory range before rejection for unstable ions (mass $A = 40$) as a function of radial entrance coordinate in the direction of instability for the three QMS designs with hyperbolic (A), circular $R = 1.16\ r_0$ (B) and circular $R = 1.127\ r_0$ rods + stabilizer rods (C). Entrance energy $E = 5$ eV, resolution $\mathcal{R} = 100$. In (a) the QMS was tuned for stability of mass 39.5 u (instability in y) and in (b) for stability of mass 40.5 u (instability in x).

variables of ion entrance energy and QMS resolution setting, further simulations have been carried out for two different ion energies ($E = 10$ eV and $E = 5$ eV) and two different resolution settings ($\mathcal{R} = 50$ and $\mathcal{R} = 100$). Quantitative results for the selectivity S for the hyperbolic QMS on the favorable high mass side are compared in Table 5. The increase in ion entrance energy by a factor of 2 leads to a deterioration of S by about four orders of magnitude, while the reduction in resolution by a factor of 2 only reduces S by a factor of 3–5. The importance of choosing the lowest possible ion entrance energy is thus clearly worked out.

3.4. Extraction and detection region

The exit region of the QMS is dominated by a focussing exit lens, set at a potential of about −100 V, and the strong accelerating potential of up to −4 kV, applied to the conversion dynode of the channeltron detector. The resulting high-energy impact of the ions striking this dynode is mandatory both for efficient production of secondary electrons and for the reduction of mass discrimination effects. The secondary electrons produced at the conversion dynode are accelerated to the front end of the channeltron detector by another potential difference of about 2 kV and subsequently multiplied to form a measurable electronic pulse. The experimental geometry is given in Fig. 12. The diagram includes a number of equipotential lines showing the field penetration into the QMS, which is significant only over a distance of about 1.5 cm. Because of this attractive potential, the full circular area of the free field radius is imaged onto the conversion dynode, excluding any transmission losses in this section of the apparatus.

Table 4
Simulated phase-averaged selectivities S determined at neighboring half mass position for the heavier mass side and the lighter mass side for the three different quadrupole designs, compared with experimental results of the instrument described in Table 1

QMS-type	Selectivity: $S = A/(A + 1/2)$	Selectivity: $S = A/(A - 1/2)$
Hyperbolic	$1.1\ (3) \times 10^{12}$	$9.1\ (1.7) \times 10^{7}$
Circular, $R = 1.16\ r_0$	$8.2\ (1.4) \times 10^{9}$	$4.2\ (8) \times 10^{6}$
Circular, $R = 1.127\ r_0$ + stabilizer rods	$7.4\ (1.3) \times 10^{10}$	$3.5\ (7) \times 10^{7}$
Experiment	$>1.1\ (3) \times 10^{8}$[a]	$3.8\ (5) \times 10^{7}$

[a]Background limited.

Table 5
Simulated phase averaged abundance selectivity S at half mass position on the heavier mass side for an ideal quadrupole with hyperbolic cross-section electrodes for two different ion entrance energies E and mass resolutions $\mathcal{R} = m/\Delta m$

	Entrance energy	
	$E = 10$ eV	$E = 5$ eV
Resolution $\mathcal{R}$	Selectivity: $S = A/(A + 1/2)$	
50	$3.7\ (8) \times 10^{7}$	$3.0\ (9) \times 10^{11}$
100	$1.8\ (3) \times 10^{8}$	$1.1\ (3) \times 10^{12}$

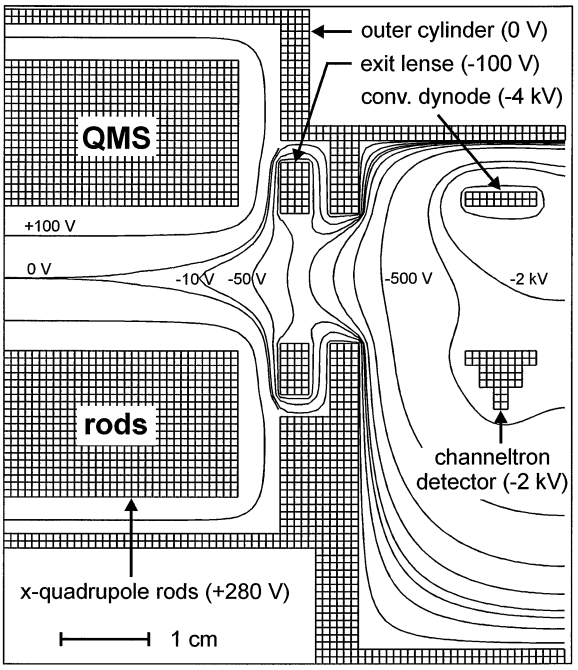

Fig. 12. Simulation of the extraction and detector region of the QMS with equipotential contour lines calculated for typical working potentials, as indicated.

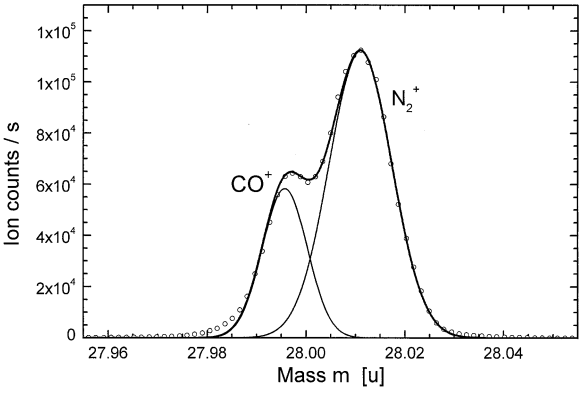

Fig. 13. Resolved mass doublet in the residual gas spectrum at mass 28 u. The fit curve is the sum of two Gaussian profiles.

4. Experimental

4.1. Experimental setup

The experimental setup used for characterization of the QMS was constructed in view of the application of the system for laser resonance ionization mass spectrometry. Analytical samples are atomized in a cylindrical graphite crucible. The crucible is coated with pyrolytic graphite and has a length of 50 mm, 4.6 mm outer diameter and ~1 mm wall thickness. The longitudinal cross section is H-shaped, such that the sample is placed at the hottest region in the middle and a self-collimated beam with full-angle divergence of less than 10° effuses out of the 20 mm deep and 2.6 mm wide exit hole. Resistive heating is performed by passing a dc current of up to 80 A longitudinally through the crucible. Calcium is placed in the crucible as an aqueous solution of calcium nitrate. At a temperature of about 1200–1500 °C calcium is efficiently reduced and evaporated. The distance between crucible exit and ionization region is ~20 mm. For the measurements described here, we used the standard crossed-beam electron impact ion source belonging to the QMS, as described in detail in Sec 3.2 and shown in Fig. 4. As discussed there, the ionization region is roughly 3 mm in diameter and 5 mm in length and is well matched to the acceptance volume of the QMS. A detailed description of the experimental parameters of the QMS has already been given (Table 1). Ions transmitted through the quadrupole structure are counted after detection by the off-axis channeltron particle multiplier. The entire QMS system consisting of ion source, quadrupole mass filter and ion counting is computer controlled using the commercial Extrel Merlin data acquisition and control electronics. The system is installed in a vacuum chamber, pumped by a turbomolecular pump, which provides residual gas pressures in the range of 10^{-7} mbar, even when the graphite crucible is heated. Additional background gases can be introduced into the system through a needle valve.

4.2. Measurements

4.2.1. Mass resolution

The maximum achievable resolution can be best demonstrated in the resolution of mass doublets with small mass difference [45]. A typical mass doublet is found in the analysis of the residual gas composition at mass number 28, composed of CO^+ at 27.9999 u and N_2^+ at 28.0134 u, with mass difference δ = 0.0135 u. Fig. 13 shows the corresponding experi-

mental measurement, where both contributions are just resolved with an intermediate valley depth of about 10% of the smaller peak. At the high resolution settings used for this measurement, the experimentally observed peak profiles are well described by a Gaussian distribution, which can be attributed primarily to the velocity distribution of the entering ions. Thus, a sum of two Gaussian distributions

$$y = \frac{1}{w_1\sqrt{2\pi}} \exp\left[-\ln 2\left(\frac{x-\bar{x}_1}{w_1/2}\right)^2\right] + \frac{1}{w_2\sqrt{2\pi}} \exp\left[-\ln 2\left(\frac{x-\bar{x}_2}{w_2/2}\right)^2\right] \quad (15)$$

accurately fits (solid curve) the experimental spectrum (points). In (15), the Gaussian width parameter w is equivalent to the peak-width Δm (FWHM). From the average for the individual peaks shown in Fig. 13, we extract $w \approx \Delta m = 0.015(2)$ u, which results in an experimentally attained resolution of $\mathcal{R}_{\text{exp}} = \bar{m}/\Delta m \approx 1900$. This value is almost a factor of 1.5 higher than the limit of $\mathcal{R}_{\text{max}} \approx 1300$ predicted by the simple approximation (12), and has been reached only by using an extremely high slope of the mass scan line of 0.9996. These conditions lead to a reduction of transmission of about two orders of magnitude when compared to a standard lower resolution setting of $\mathcal{R} = 100$.

4.2.2. Isotopic abundance sensitivity

For the measurement of abundance sensitivity as well as precise isotope ratios, it is highly desirable to suppress background ionization as much as possible. For this purpose, we have performed detailed studies of the relative efficiencies for electron impact ionization of different species, present either as residual gases or produced during heating of the calcium-filled graphite crucible, as a function of electron impact energy. These measurements have shown that a rather selective ionization of calcium atoms, avoiding most molecular interferences, can be achieved when the electron energy is chosen to be 12–15 eV. Because of calcium's relatively low ionization potential (IP_{Ca} = 6.11 eV), it is still efficiently ionized [24] at these

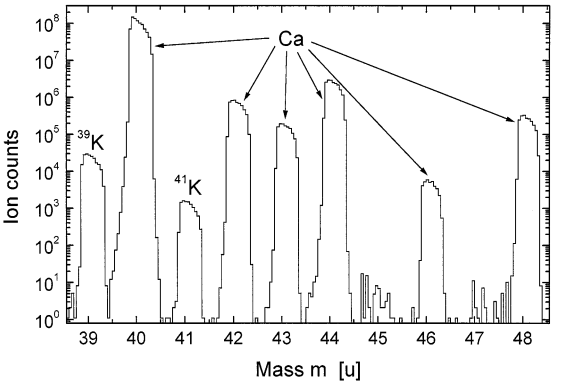

Fig. 14. High-dynamic-range mass spectrum in the range of calcium obtained using selective electron impact ionization.

energies, while molecular species are not. The ionization efficiency of Ca is reduced only by a factor of about 3 when reducing electron impact energy from 25–12 eV, while the molecular interference from CO_2^+ at mass 44 is reduced by four orders of magnitude. In principle, the relative preferential ionization of calcium can be increased even further at lower electron energies, however, this can be accomplished only at the expense of rapidly decreasing absolute efficiency.

A typical high-dynamic-range mass spectrum over the mass range of the calcium isotopes, taken under the conditions outlined above, is shown in Fig. 14. The spectrum is the sum of 135 scans with a dwell time of 1 s per channel, an electron impact energy of 14 eV, an ion energy of 5 eV and a resolution of about 100. The dark-count background rate of the channeltron detector is ~5 mHz, corresponding to an average of ~0.5 counts per channel over the total measurement time of eight hours. Very weak background peaks are observed at 45 u (possibly $^{44}CaH^+$) and possibly 47 u (unknown), while stronger peaks occurring at 39 u and 41 u are assigned to potassium. Because the ionization potential of potassium (IP_K = 4.34 eV) is lower than that of calcium, it cannot be suppressed by the low electron energy method. Even after careful cleaning and preparation of the graphite furnace and calcium sample, typical K contributions of 10^{-4}–10^{-5} of calcium were observed. Thus, for the planned determination of ^{41}Ca with a natural abun-

dances of less than 10^{-14}, this illustrates the need for complete isobaric suppression which can be achieved with a laser resonance ionization process.

Integration over the channels located at the position of mass 39.5, 40 and 40.5 u yields experimental values for the neighboring half-mass suppression of the QMS system under investigation. At a half-mass unit on the lighter mass side a value of $S \approx 3.8(5) \times 10^7$ is obtained, while on the heavier mass side it is $S \approx 1.1(3) \times 10^8$. The value on the lower mass side is in excellent agreement with the abundance sensitivity predicted by the ion trajectory simulations in Sec. 3.6. The experimental value on the heavier mass side appears to be limited by background, primarily the dark count rate of the channeltron, rather than by true wings of the ^{40}Ca peak. It is also possible that there are small contributions from gas kinetic collisions, which are discussed below. Because measurements with even higher dynamic range are exceedingly difficult and time consuming, this number is taken as an upper bound on the maximum interference to be expected from ^{40}Ca during ^{41}Ca determinations.

4.2.3. Gas kinetic collisions inside the QMS

The influence of residual gas collisions can be estimated from the simulations using a simple assumption. Under the typical vacuum conditions of $\leq 5 \times 10^{-7}$ mbar, the probability of multiple collisions occurring during transmission through the QMS is negligible. Thus, each ion on an unstable trajectory, which is detected as background after a collision with a residual gas molecule, must have travelled (either before or after the collision) at least half of the QMS length on a trajectory without rejection. Thus a rough estimate of the probability of detecting such an ion is given by the product of the selectivity of a 10.5 cm length QMS (about 10^{-4} for the heavier mass side and 10^{-3} for the lighter mass side), the probability for collision at the given vacuum conditions (about 10^{-3}), and the averaged probability of this collision resulting in detection of the ion ($\leq 10^{-2}$). The latter is based on geometrical considerations on the distance and size of the detector assuming equally distributed scattering angles because of the high radial ion velocity. The resulting product is only about 10^{-9} for the heavier mass side and 10^{-8} for the lower mass side and thus is below what can be observed with the available experimental dynamic range. Nevertheless, by artificially increasing the vacuum by an order of magnitude up to 5×10^{-6} mbar we could demonstrate this effect on the experimentally observed selectivities. The selectivity values observed under these conditions were reduced from those given in Table 4 only slightly from 3.8×10^7 to 3×10^7 on the lower mass side but about a factor of 3 from 1.1×10^8 to 4×10^7 on the heavier mass side. This behavior is at least qualitatively in accordance with expectations and is probably the limiting mechanism for selectivity that can be experimentally realized on the heavier mass side.

4.2.4. Isotope ratio measurements

For precise isotope ratio determination with a QMS, there are a number of experimental factors which must be taken into account. Almost every process involved in the measurement exhibits mass discrimination effects to some extent. Thus, attempts were made to consider all known effects caused by experimental conditions: These include different ionization probability because of the mass dependent velocity of the entering atoms, corrections for counter dead-time characteristics [46], as well as a number of poorly understood mass dependent effects such as the effect of fringe fields on QMS transmission and secondary electron efficiency in the detector. Generally, these latter effects must be evaluated collectively and empirically with calibration samples.

The mass dependent thermal velocity for different isotopes entering the ionization region leads to shorter interaction times for lighter isotopes. This effect can be corrected simply by normalizing inversely proportional to the square root of the masses. The mass discrimination caused by fringing fields of the QMS [22] is usually linear over smaller mass ranges and can be corrected by a mass dependent setting of the entrance lens. The residual effects, after these corrections, were analyzed in the mass spectrum of calcium by assuming the well known natural isotopic composition (compare Table 2). These studies concentrated on the ratios of the minor stable calcium isotopes,

Table 6
Experimentally determined minor calcium isotope ratios and reference values (from [36])

Isotope ratio	This work	Reference values [36]	% deviation between this work and [36]
43/42	0.2081 (2)	0.207 74 (3)	−0.17 (10)
44/42	3.2134 (8)	3.2030 (2)	−0.32 (3)
46/42	0.004 86 (2)	0.004 862 (6)	0.04 (43)
48/42	0.2853 (2)	0.284 19 (3)	−0.39 (7)

$^{42-44,46,48}$Ca. Integration of total ion counts under the individual mass peaks for a number of measurements similar to that shown in Fig. 14, but excluding the 97% abundant ^{40}Ca, and with varying statistics were performed. The resulting isotope ratios of ^{43,44,46,48}Ca to ^{42}Ca are given in Table 6 and compared to reference values [36]. In all cases the relative discrepancy is less than 0.4%, but is still somewhat larger (except for the 3×10^{-5} abundant ^{46}Ca) than the statistical uncertainty. The small remaining discrepancies may be ascribed to residual molecular interferences and possibly small uncompensated mass discrimination effects. Further studies, using selective laser ionization to avoid isobaric interferences, are planned to reevaluate the maximum precision achievable with this QMS system.

5. Summary

The performance of a standard commercial QMS system, which is used for highly selective laser resonance ionization has been analyzed. Ion trajectory simulations with the computer code SIMION 3D version 6.0 were performed, giving detailed insight into the behavior and flight trajectories of ions within the fields of a circular rod QMS. The simulations show that the field approximation of different commercial QMS designs with circular cross-section electrodes as compared to the ideal hyperbolic field depends strongly on the ratio of electrode radius to free field radius and can be further optimized by installing additional grounded stabilizer rods. These stabilizer rods lead to a sixfold reduction in the field deviation over the central region and to an one order of magnitude improvement in abundance sensitivity, when compared to a standard circular electrode design. The dependence of mass filter resolution and abundance sensitivity on different experimental parameters such as ion entrance energy, rf phase, and the slope of the mass scan line were estimated using the simulations. Comparing these results with experimental measurements using conventional electron impact ionization demonstrate that the theoretical predictions of high resolution in the range of $m/\Delta m > 1500$ and extremely high isotopic abundance sensitivity of more than 10^8 can be achieved in a commercial quadrupole mass spectrometer simply by optimizing standard working parameters. The agreement of the experimental data with the simulation is generally very good. Isotope ratio measurements with precision of better than 0.5% are possible. Combining the isotopic abundance sensitivity of this QMS system with the optical selectivity that has been demonstrated for laser ionization of ^{41}Ca [31,34], it should be possible to achieve overall isotopic selectivity of $>10^{13}$ for applications requiring the measurement of this long-lived radionuclide. Similar performance can be expected for a wide variety of other problems that can be addressed with selective ultratrace determination by laser resonance ionization mass spectrometry [30].

Acknowledgements

The authors would like to thank Dr. R. E. Pedder and G. York from ABB Extrel for stimulating discussions. Funding from the Deutsche Forschungsgemeinschaft and the “Zentrum für Umweltforschung der Johannes Gutenberg-Universität Mainz” is gratefully acknowledged.

References

[1] W. Paul, H. Steinwedel, Z. Naturforschung. 8a (1953) 448.
[2] W. Paul, M. Raether, Z. Phys. 140 (1955) 162.
[3] W. Paul, H.P. Reinhard, U. von Zahn, Z. Phys. 152 (1958) 143.

[4] W. Paul, H. Steinwedel, Ger. Pat. 944, 900 (1956); US Pat. 2,939,952 (1960).
[5] F. von Busch, W. Paul, Z. Phys. 164 (1961) 588.
[6] W.M. Brubaker, Proc. Int. Conf. Instrum. Meas. 1 (1961) 305.
[7] W.M. Brubaker, J. Tuul, Rev. Sci. Instrum. 35 (1964) 1007.
[8] W.M. Brubaker, Adv. Mass Spectrom. 4 (1968) 293.
[9] D.R. Denison, J. Vac. Sci. Technol. 8 (1971) 266.
[10] G.E. Lee-Whiting, L. Yamazaki, Nucl. Instrum. Methods 94 (1971) 319.
[11] H.F. Dylla, J.A. Jarrell, Rev. Sci. Instrum. 47 (1976) 331.
[12] W.E. Austin, J.H. Leck, J.H. Batey, J. Vac. Sci. Technol. A 10 (1992) 3563.
[13] V.V. Titov, J. Am. Soc. Mass Spectrom. 9 (1998) 50.
[14] V.V. Titov, J. Am. Soc. Mass Spectrom. 9 (1998) 70.
[15] P.H. Dawson, N.R. Whetten, Int. J. Mass Spectrom. Ion Phys. 3 (1969) 1.
[16] F. Muntean, Int. J. Mass Spectrom. Ion Processes 151 (1995) 197.
[17] A.J. Reuben, G.B. Smith, P. Moses, A.V. Vagov, M.D. Woods, D.B. Gordon, R.W. Munn, Int. J. Mass Spectrom. Ion Processes 154 (1996) 43.
[18] J.J. Tunstall, A.C.C. Voo, S. Taylor, Rapid Commun. Mass Spectrom. 11 (1997) 184.
[19] E.W. Blauth, Dynamic Mass Spectrometers, Elsevier, Amsterdam, 1966, pp. 119–137.
[20] F.A. White, Mass Spectrometry in Science and Technology, Wiley, New York, 1968, pp. 66–107.
[21] P.H. Dawson, N.R. Whetten, Adv. Electron. Electron Phys. 27 (1969) 59.
[22] Quadrupole Mass Spectrometry and its Applications, Elsevier, Amsterdam, 1976.
[23] R.E. March, R.J. Hughes, J.F.J. Todd, Quadrupole Storage Mass Spectrometry, Wiley, New York, 1989, pp. 31–110.
[24] B.A. Bushaw, B.D. Cannon, G.K. Gerke, T.J. Whitaker, Opt. Lett. 11 (1986) 422.
[25] B.A. Bushaw, F. Juston, W. Nörtershäuser, N. Trautmann, P. Voss-de Haan, K. Wendt, in N. Winograd and J.E. Parks (Eds.), Multiple Resonance RIMS Measurements of Calcium Isotopes Using Diode Lasers, RIS 96, AIP Conference Proceedings 388, Woodbury, New York, 1996, p. 115.
[26] Applied Laser Spectroscopy, D.L. Andrews (Ed.), VCH, New York, 1992.
[27] Laser Ionization Mass Analysis, A. Vertes, R. Gijbels, F. Adams (Eds.), Wiley, New York, 1993.
[28] B.A. Bushaw, B.D. Cannon, Spectrochim. Acta B 52 (1997) 1839.
[29] K. Wendt, K. Blaum, B.A. Bushaw, F. Juston, W. Nörtershäuser, N. Trautmann, B. Wiche, Fresenius J. Anal. Chem. 359 (1997) 361.
[30] K. Wendt, in J. Parks, J. Vickerman and I. Lyon (Eds.), Ultratrace Determination of Long-lived Radioactive Isotopes, RIS 98, AIP, Woodbury, in press.
[31] P. Müller, B.A. Bushaw, K. Blaum, W. Nörtershäuser, N. Trautmann, K. Wendt, in J. Parks, J. Vickerman and I. Lyon (Eds.), Ultratrace Determination of the Long-lived Isotope ^{41}Ca by Narrowband CW-RIMS, RIS 98, AIP, Woodbury, in press.
[32] W. Kutschera, Nucl. Instrum. Methods Phys. Res. B 123 (1997) 594.
[33] W. Nörtershäuser, N. Trautmann, K. Wendt, B.A. Bushaw, Spectrochim. Acta B 53 (1998) 709.
[34] B.A. Bushaw, W. Nörtershäuser, K. Wendt, Spectrochim. Acta B, submitted.
[35] D.A. Dahl, SIMION 3D 6.0. Ion Source Software, Idaho National Engineering Laboratory, 1995.
[36] F.R. Niederer, D.A. Papanastassiou, Geochim. Cosmochim. Acta 48 (1984) 1279.
[37] M. Paul, I. Ahmad, W. Kutschera, Z. Phys. Z 340 (1991) 249.
[38] G.M. Raisbeck, F. Yiou, Nature 277 (1979) 42.
[39] I.E. Dayton, F.C. Shoemaker, R.F. Mozley, Rev. Sci. Instrum. 25 (1954) 485.
[40] N.W. McLachlan, Theory and Application of Mathieu Functions, Clarendon, Oxford, 1947.
[41] R.E. March, J. Mass Spectrom 32 (1997) 351.
[42] R. Alheit, Th. Gudjons, S. Kleineidam, G. Werth, Rapid Commun. Mass Spectrom. 10 (1996) 583.
[43] R. Alheit, S. Kleineidam, F. Vedel, M. Vedel, G. Werth, Int. J. Mass Spectrom. Ion Processes 154 (1996) 155.
[44] V.S. Letokhov, Laser Photoionization Spectroscopy, Academic, Orlando, 1987, pp. 89–92.
[45] F.A. White, G.M. Wood, Applications in Science and Engineering, Wiley, New York, 1986, pp. 161–172.
[46] G.F. Knoll, Radiation Detection and Measurement, Wiley, New York, 1979, pp. 95–102.